Regular Article

Porous ZrO$_2$ encapsulated perovskite composite oxide for organic pollutants removal: Enhanced catalytic efficiency and suppressed metal leaching
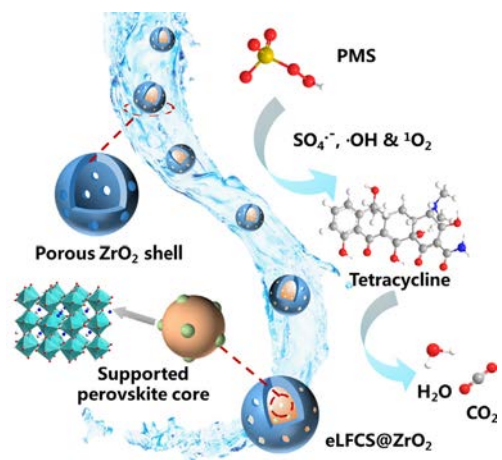
Longfei Zhang, Luhong Zhang, Yongli Sun, Bin Jiang *

School of Chemical Engineering and Technology, Tianjin University, Tianjin 300072, PR China

GRAPHICAL ABSTRACT

The rational design of the core-shell structure can not only facilitate the degradation of the pollutants but also inhibit cobalt ion leaching of cobalt-based perovskite material.

ARTICLE INFO

ABSTRACT

Cobalt-based perovskite material, an effective activator of PMS, is widely employed for wastewater remediation, but still affected by the leakage of the cobalt ions. In this study, a porous core-shell structured perovskite LaFe$_{0.1}$Co$_{0.9}$O$_{3-\lambda}$/SiO$_2$ core @ZrO$_2$ shell (LFCS@ZrO$_2$) was fabricated and partially etched to enlarge channels to further enhance mass transfer ability. The well-designed core-shell structure can not only restrain metal ion leaching by changing the surface microenvironment but also provide an additional driving force attributed to the enriched concentration gradient, thus enhancing the catalytic oxidation performance. Results showed that the partially etched LFCS@ZrO$_2$ (eLFCS@ZrO$_2$) particles exhibited an increased pore size and showed an attractive catalytic performance as well as a suppressed cobalt ion leaching (3.61 to 0.67 mg/L). Over 99% of tetracycline hydrochloride (20 mg/L) could be degraded in 15 min, and the reaction rate increased 2 folds compared with pristine LaFe$_{0.1}$Co$_{0.9}$O$_{3-\lambda}$. Besides, quenching test and electron paramagnetic resonance analysis proved that sulfate radicals and singlet oxygen were the two predominant reactive oxygen species during the catalytic oxidation. This work provides

* Corresponding author.
    E-mail address: binj@tju.edu.cn (B. Jiang).

a novel perspective for the fabrication of an environmentally friendly perovskite catalyst, which has a great potential application in organic pollutant degradation.

1. Introduction

The widespread use of antibiotics has led to an irreversible impact on the environment due to their non-degradable characters. In particular, tetracycline hydrochloride (TC) as an emerging contaminant has been detected in water bodies and poses a potential threat to environment and human beings even at trace concentrations. Traditional adsorption and biological methods are inefficient with the improvement of the water quality standards [1–3].

Nowadays, advanced oxidation process with deep mineralization capacities has received extensive attention toward antibiotic degradation. In particular, sulfate radical based advanced oxidation process exhibits attractive catalytic oxidation efficiency due to the highly reactive radicals [1,4,5]. Sulfate radicals (SO_4^-) generated by activation of peroxymonosulfate (PMS) possess higher redox potential (2.5–3.1 V vs 2.8 V), longer half-life period (30–40 ms vs 20 ns), and wider pH range (2–8) compared with hydroxyl radicals (·OH). Besides, SO_4^- tend to react with aromatic compounds via electron transfer and have become a heated topic in recent research [6–8]. However, the heterogeneous catalysts used for PMS activation are mainly dominated by transition metal oxides. Among them, cobalt oxide performs optimal activation efficiency [9–11]. However, cobalt ion leaching is an urgent problem that must be solved during the PMS activation process, because minor amount of cobalt ions are capable to cause a serious impact on environment [12,13]. Extensive efforts have been paid to overcome this problem. One of the most effective methods is to prepare a cobalt-based catalyst with a bimetal structure like perovskite or spinel [14–16]. Owing to the bonding between two metal ions, the stability of the catalyst is enhanced [17]. Moreover, the tuning structure of perovskite enables its attractive catalytic efficiency and stability, which shows expected merits in PMS-based catalytic oxidation [18–20]. For example, Fe doped perovskite $LaFe_xCo_{1-x}O_{3-\lambda}$ deposited SiO_2 was prepared for TC degradation and results showed that the TC removal efficiency is improved owing to the oxygen vacancies and promoted electron transfer. Besides, the catalyst also performed attractive stability [20]. Lu et al. fabricated a copper doped $LaCoO_3$ perovskite for phenol degradation, which exhibited favorable catalytic efficiency and stability [17]. However, the prerequisite of catalytic oxidation, adsorption of pollutant on catalyst surface is constrained by low specific surface area (SSA) of perovskite. Besides, catalysts are still in contact with PMS directly along with the catalytic oxidation process and acidic environment generated during the reaction has a marked impact on cobalt ion leaching [9,21]. Therefore, the rational development of catalysts to prevent metal leaching is of great importance.

Functional catalysts with a core-shell structure have shown favorable performance in terms of catalytic oxidation and a variety of applications [22,23]. On account of the different divisions of core-shell structure, catalytic performance can be further promoted by the synergistic effects of the core and shell. Namely, the active sites of the catalyst are encapsulated by a porous shell, preventing direct contact between active sites and external environment. Besides, micro-environment around catalyst is optimized because of the improved adsorption capacity toward target pollutants, providing an additional driving force from the enriched concentration gradient. More importantly, owing to the protection of the shell structure, the stability of catalyst is improved and metal leaching can be prevented simultaneously [24–26]. For example, Zhang et al. prepared a core-shell structured $CoN/N—C@SiO_2$ catalyst with dual active sites for TC degradation. Results showed that the core-shell structure increased both stability and catalytic efficiency of catalyst [24]. Besides, a yolk-shell $Co_3O_4/C@SiO_2$ nanoreactor was fabricated for degrading bisphenol A via activating PMS, which exhibited favorable stability owing to the core-shell structure, and the reaction kinetic was also improved [25]. However, active components of catalyst, mainly monometallic oxides, are constrained by its stability and catalytic efficiency. Therefore, the catalytic oxidation is limited to a certain extent. Zirconium dioxide (ZrO_2) has been widely employed as a candidate to form core-shell structured particles in a variety of applications due to its high SSA, stability, abundant surface defects, as well as the weak acid and alkalinity characters [27]. The unique surface structure enables it more suitable to act as a support material or shell candidate, and can also be recognized as an auxiliary to improve the catalytic efficiency and stability of catalysts [28]. In this regard, employing high efficient perovskite material as the core and ZrO_2 as a shell can not only improve catalytic efficiency and stability of catalyst but also reduce cobalt ion leaching with eco-friendly characteristics.

In this study, to enhance catalytic efficiency and suppress cobalt ion leaching of the catalytic oxidation processes, a perovskite $LaFe_{0.1}Co_{0.9}O_{3-\lambda}/SiO_2@ZrO_2$ (LFCS@ZrO$_2$) was prepared by sol-gel, incipient impregnation, and was partially etched by alkaline aqueous solution. The structure and element composition of the partially etched LFCS@ZrO$_2$ (eLFCS@ZrO$_2$) particle were characterized and formation parameters such as the mass proportion of core to shell, etching time, etc. were investigated. The catalytic oxidation performance of the eLFCS@ZrO$_2$ was researched using TC degradation efficiency as the indicator by activating PMS. The influences of conditions such as temperature, catalyst dosage, pH value, etc. were also considered in detail. Furthermore, cycling abilities, cobalt ion leaching, and mechanisms of the catalysts were systematically evaluated.

2. Experimental

2.1. Chemical and reagents

Lanthanum nitrate hexahydrate ($La(NO_3)_3·6H_2O$, AR grade, 99%), ferric nitrate nonahydrate ($Fe(NO_3)_3·9H_2O$, AR grade, 99%), cobalt nitrate hexahydrate ($Co(NO_3)_2·6H_2O$, AR grade, 99%), cetyltrimethylammonium bromide (CTAB, AR grade, 99%), citric acid ($C_6H_8O_7$, AR grade, 99%), sodium hydroxide (NaOH, AR grade, 99%), aqueous ammonia ($NH_3·H_2O$, AR grade, 28%) and tetracycline hydrochloride (TC, AR grade, 99%) were purchased from Tianjin Guangfu Fine Chemical Research Institute. Methanol (MeOH, AR grade, 99%), *tert*-butyl alcohol (TBA, AR grade, 99%), L-histidine (L-his, AR grade, 99%), tetraethyl orthosilicate (TEOS, AR grade, 99%), zirconium oxychloride octahydrate ($ZrOCl_2·8H_2O$, AR grade, 99%) and peroxymonosulfate ($2KHSO_5·KHSO_4·K_2SO_4$, AR grade) were purchased from Aladdin Industrial Corporation. All chemicals were used without further purification.

2.2. Preparation of LFCS particles

To obtain the functional particle with an optimized core-shell structure, the prerequisite is to improve the dispersion and reduce

the agglomeration phenomenon. Therefore, SiO_2 support was introduced to improve the dispersion of the $LaFe_{0.1}Co_{0.9}O_{3-\lambda}$. The LFCS was prepared by incipient impregnation method according to literature [20]. Typically, 2.0 mmol $La(NO_3)_3 \cdot 6H_2O$, 0.2 mmol $Fe(NO_3)_3 \cdot 9H_2O$, 1.8 mmol $Co(NO_3)_2 \cdot 6H_2O$ and 6 mmol citric acid were dissolved in 10 mL deionized water, and the pH was adjusted to 9.0 by ammonia. Afterwards, the mixed solution was introduced dropwise to 2.0 g SiO_2 support under ultrasonic and oscillated for 4 h. The as-prepared particle was dried overnight at 60 °C. Finally, the as-prepared particles were calcined in air at 700 °C for 4 h and ground prior to use.

2.3. Preparation of eLFCS@ZrO2

The core-shell structured $LFCS@ZrO_2$ was prepared through the hydrolysis of $ZrOCl_2 \cdot 8H_2O$. In a typical synthesis, 0.2 g LFCS was dispersed in 80 mL deionized water, and 0.1 g CTAB was introduced into the solution under vigorous stirring. After rectifying the pH to 9.0 by ammonia solution, 0.8 mmol of $ZrOCl_2 \cdot 8H_2O$ was dissolved in 20 mL deionized water and added dropwise under continuous stirring for 2 h to form the ZrO_2 shell. The obtained particle was then dried at 60 °C overnight and calcined in air at 550 °C for 5 h to remove CTAB and form a porous shell structure. The weight ratio of the ZrO_2 shell and LFCS core was set as 1:3, 1:4, and 1:5. The $eLFCS@ZrO_2$ was prepared via an alkaline-induced etching process. Briefly, 0.2 g $LFCS@ZrO_2$ was dispersed in 50 mL 1 mol/L NaOH aqueous solution and heated at 30 °C for several hours under continuous stirring. Thereafter, the resulting particles were collected by filtration and washed by ethanol and deionized water several times, and then dried prior to use.

2.4. Analytical methods

X-ray diffractometer (XRD. D8 Advance, Germany) was employed to analyze the crystal structure of samples with a 2θ range of 20°-80°, and scanning rate was 5°/min. Fourier transform infrared spectrometry (FT-IR, AVATAR 360, USA) was performed to analyze the functional groups of the samples. The morphology and element composition of the samples were observed by scanning electron microscope (SEM, Hitachi S4800, Japan) and energy dispersive spectrometer (EDS) mapping. Transmission electron microscope (TEM, JEM-2100F, Japan) was used to determine the structure and crystal lattice of the samples. X-ray photoelectron spectrometer (XPS, ESCALAB 250Xi, UK) was employed to test the surface elemental composition. The SSA of the samples was measured by a Brunauer-Emmett-Teller analyzer (BET, Tristar 3000, USA). The electrochemical measurement was carried out in a three-electrode system using Ag/AgCl as the reference electrode and Pt electrode was employed as the counter electrode, besides, 0.05 mol/L Na_2SO_4 aqueous solution was used as the electrolyte solution. The electrochemical impedance spectroscopy (EIS) performance was performed in the frequency of 10^5 to 0.01 Hz, and the amplitude was 0.05 V. Cyclic voltammetry (CV) curves were identified between the voltage range from −1 to 1.8 V and the scan rate was 0.05 V/s [29,30]. The TC concentration was measured by an ultraviolet spectrophotometer (UV-spectrum, SP-752, China) with a wavelength of 357 nm. The concentration of cobalt ions was manifested by an inductively coupled plasma optical emission spectroscopy (ICP-OES, VISTA-MPX, USA). The chemical oxygen demand (COD) and total organic carbon (TOC) of the initial and treated TC aqueous solution were tested by a COD analyzer (COD-571, Shanghai, China) and a TOC-L analyzer (TOC, Shimadzu, Japan). The intermediate products of the TC degradation were identified by a UHPLC-MS (Ultimate 3000 UHPLC-Q Exactive, US) spectrum. The zeta potential of the catalyst was analyzed by a zeta potential analyzer (Zetasizer Nano ZS90, UK). Besides, the gener-

ated radicals or non-radicals were analyzed by an electron paramagnetic resonance (EPR, EMXPLUS, German) using 5,5-dimethyl-1-pyrroline-N-oxide (DMPO) and 2,2,6,6-tetramethylpiperidine (TEMP) as spin-trapping agents.

2.5. Catalytic activity evaluation

The catalytic performance was evaluated using TC degradation as an indicator. Typically, 10 mg catalyst was introduced into 100 mL TC aqueous solution (20 mg/L) and stirred for 5 min to assist the adsorption of the TC on the catalyst surface. Afterwards, 1.0 mM PMS was added into the above solution under continuous magnetic stirring. The sample was withdrawn at predetermined time intervals by a syringe, filtrated by 0.22 μm microfiltration membrane, and tested by the UV-spectrum. Besides, additional conditions such as PMS concentration, catalyst dosage, temperature, initial pH, and effects of the foreign ions were investigated in detail. Radical quenching test was also performed to reveal the generation of the free radicals and non-radicals by using MeOH, TBA, and L-his as radical scavengers. To identify the reaction rate, pseudo-first-order kinetics equation was employed to verify the catalytic performance of samples.

$$\ln \frac{C}{C_0} = -kt \tag{1}$$

Where C_0 and C represent the TC concentration before and after treatment (mg/L), k is the reaction rate constant (min^{-1}), and t means the reaction time (min).

3. Results and discussion

3.1. Morphology and structure of functional particles

The morphology of the functional particle is shown in Fig. 1. As shown in Fig. 1(a), the LFCS exhibited good sphericity, and the agglomeration phenomenon was obvious due to the loaded perovskite $LaFe_{0.1}Co_{0.9}O_{3-\lambda}$. Besides, morphologies of $LFCS@ZrO_2$ and $eLFCS@ZrO_2$ also showed attractive sphericity, but surface roughness slightly increased. When $LFCS@ZrO_2$ was partially etched by NaOH aqueous solution, the structure of $eLFCS@ZrO_2$ was almost unaltered and the agglomeration was meliorated. Fig. 1(d-e) depicts the TEM images of $eLFCS@ZrO_2$. The observed $eLFCS@ZrO_2$ showed a typical core-shell structure compared with TEM image of LFCS (Fig. S1), and the thickness of the ZrO_2 shell was about 10–15 nm. Moreover, the core structure of the $eLFCS@ZrO_2$ was partially destroyed and more perovskite active sites were exposed and then encapsulated by the ZrO_2 shell, which resulted in an improved catalytic efficiency. High-resolution TEM image is also provided to prove the structure of perovskite, the interlayer distance of 0.383 nm was corresponding to the (1 1 0) planes of $LaFe_{0.1}Co_{0.9}O_{3-\lambda}$, proving the formation of the perovskite on core structure. EDS mapping depicted in Fig. 1(f-l) also illustrated the uniform distribution of the elements in $eLFCS@ZrO_2$ structure, and the element composition is shown in Fig. S2.

The FT-IR spectrums of catalysts are illustrated in Fig. 2(a). The spectrum of LFCS showed a board band at around 3440 cm^{-1}, which was caused by the surface hydroxyl group on SiO_2 support. Besides, the peaks located at 1110, 810, and 472 cm^{-1} were corresponding to the Si-O-Si asymmetric stretching vibration, Si-O-Si bridge, and deformation of Si-O-Si bridges, respectively [31]. The band centered at around 606 cm^{-1} was related to the metal-oxygen stretching vibration of the octahedrons BO_6^- in the perovskite structure [32]. However, due to the relatively low ratio of perovskite to SiO_2 support, the peak at 606 cm^{-1} performed less intense features. When coated by ZrO_2, the band intensity of SiO_2
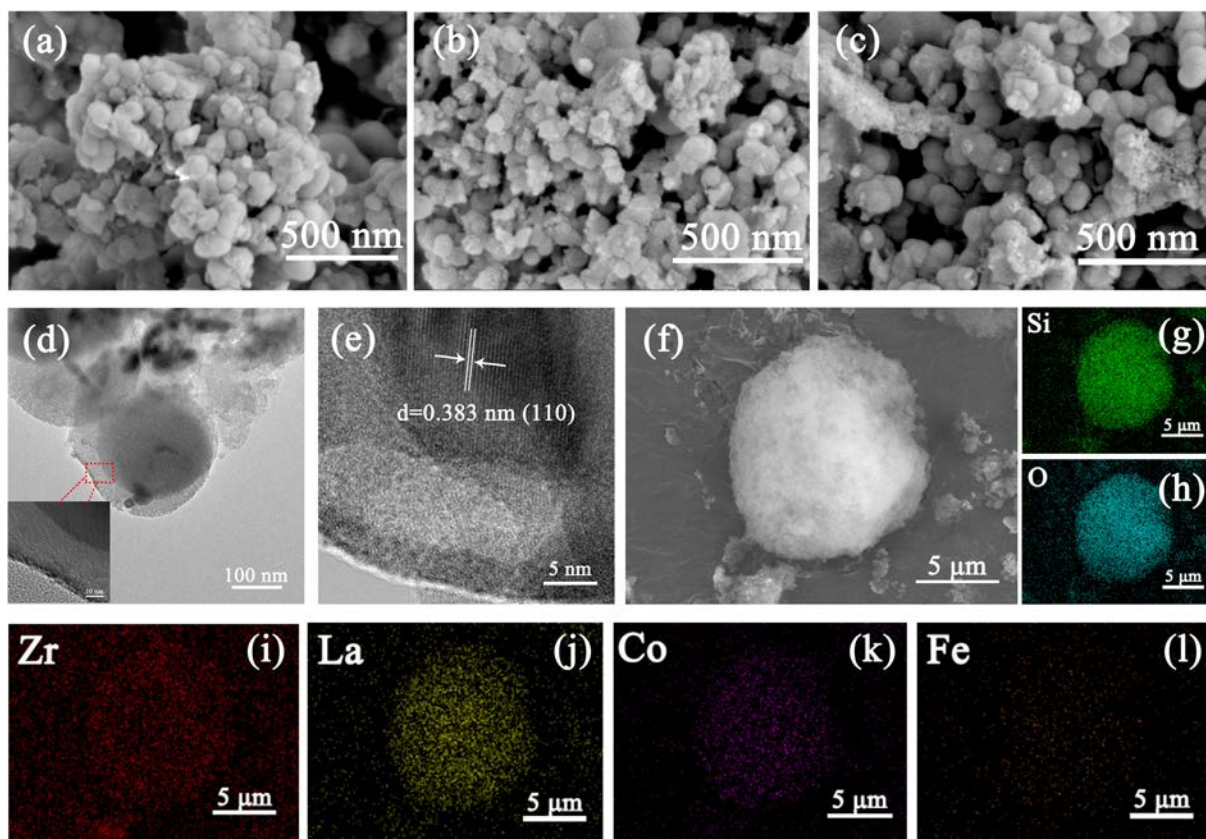
Fig. 1. Morphology of functional particles. SEM image of LFCS (a); LFCS@ZrO$_2$ (b); eLFCS@ZrO$_2$ (c); TEM images of eLFCS@ZrO$_2$ (d-e) and EDS mapping of eLFCS@ZrO$_2$ (f-l).

decreased. Notably, the bandwidth declined at 1110 cm^{-1}, which was ascribed to the formation of Si-O-Zr bond forming at the calcination process [31]. For the etched samples, the bandwidth at 1110 cm^{-1} further decreased due to the partially hydrolyzed SiO$_2$, and the character band intensity of perovskite at 606 cm^{-1} increased simultaneously. Besides, the FT-IR spectrum of ZrO$_2$ is depicted and described in Fig. S3.

The XRD patterns of the catalysts are depicted in Fig. 2(b), the diffraction pattern of LFCS was consistent with perovskite LaCoO$_3$ (PDF card No. 84-0848), indicating the amorphous structure of the SiO$_2$ support and a small amount of Fe doping did not change the crystal structure of LFCS. The characteristic peaks centered at 2θ = 23.2°, 32.9°, 40.6°, 47.5°, and 58.9° were in line with (1 1 0), (−1 1 0), (0 2 0), (1 2 0) and (1 3 0) planes. Besides, no other metal oxide crystal structure was found, proving that the main active component of the catalyst was the perovskite. When ZrO$_2$ was coated on LFCS to form a core-shell structure, the position of the LFCS@ZrO$_2$ characteristic peak was almost unaltered, but with an obvious decrease in peak intensity caused by the inhibition of the ZrO$_2$ shell. Furthermore, it was worth noting that the characteristic peaks of monoclinic and tetragonal ZrO$_2$ did not appear on the XRD pattern of LFCS@ZrO$_2$. Two reasons were put forward to explain this interesting phenomenon: 1) the formation of Si-O-Zr bond stabilized the amorphous structure of ZrO$_2$; 2) the low-expansivity of SiO$_2$ hindered the ZrO$_2$ particle growth, and postponed the crystallization of ZrO$_2$ to a higher temperature [31]. The peak intensity of eLFCS@ZrO$_2$ remained unchanged after partially etching SiO$_2$, which demonstrated favorable stability of perovskite material [33]. The N$_2$ adsorption/desorption isotherms of the various functional particles are shown in Fig. 2(c). All the curves represented a typical IV-type isotherm together with a sharp capillary condensation step. The SSA of LFCS was 17.61 m^2/

g. However, when LFCS was encapsulated by a porous ZrO$_2$ shell, SSA increased dramatically to 270.36 m^2/g with a board pore size distribution centered at around 9.5 nm. In contrast, the eLFCS@ZrO$_2$ sample exhibited a smaller SSA (205.96 m^2/g). At the same time, a wider pore size distribution can be observed and the mean pore size was concentrated at around 18.2 nm. This phenomenon can be explained by the following reasons: the SiO$_2$ support was partially etched by NaOH solution, which induced certain gaps between perovskite LaFe$_{0.1}$Co$_{0.9}$O$_{3-\lambda}$ and ZrO$_2$ shell, improving the pore size of the catalyst. On the one hand, the relative high SSA endowed sufficient reaction site for the adsorption of pollutant on the catalyst surface; on the other hand, due to the enlarged mesoporous structure, the concentration gradient significantly increased during the reaction process according to Fick's first law, especially at the initial stage, enabling a vigorous driving force for pollutant degradation and enhanced mass transfer simultaneously. XPS analysis was utilized to comprehend the surface element composition and the valance state of the active metal ions. Besides, XPS survey scans of LFCS and eLFCS are shown in Table S1. Signals of La, Co, Fe, O, and Si can be found in the full-scale XPS spectra of LFCS while Zr element was detected in eLFCS@ZrO$_2$ spectra (Fig. 2(d)).

The high-resolution XPS spectrums of Co 2p and O 1s are shown in Fig. 3(a). For Co 2p spectrum, two broad peaks located at around ~780.5 and ~795.9 eV were assigned as Co 2p$_{3/2}$ and Co 2p$_{1/2}$ spin-orbit lines. Besides, two satellite peaks were also identified in Co 2p spectrum. The doublet peaks at around ~780.3 and ~795.4 eV was attributed to Co^{3+}, while the peaks at around ~782.2 and ~797.3 eV were recognized as Co^{2+}. The relative atomic ratios of Co^{3+} to Co^{2+} were 74.2% and 25.8% for LFCS, while that for eLFCS@ZrO$_2$ were 68.1% and 31.9%. According to previous research, higher relative ratio of Co^{3+} to Co^{2+} resulted in oxygen vacancy density [34].
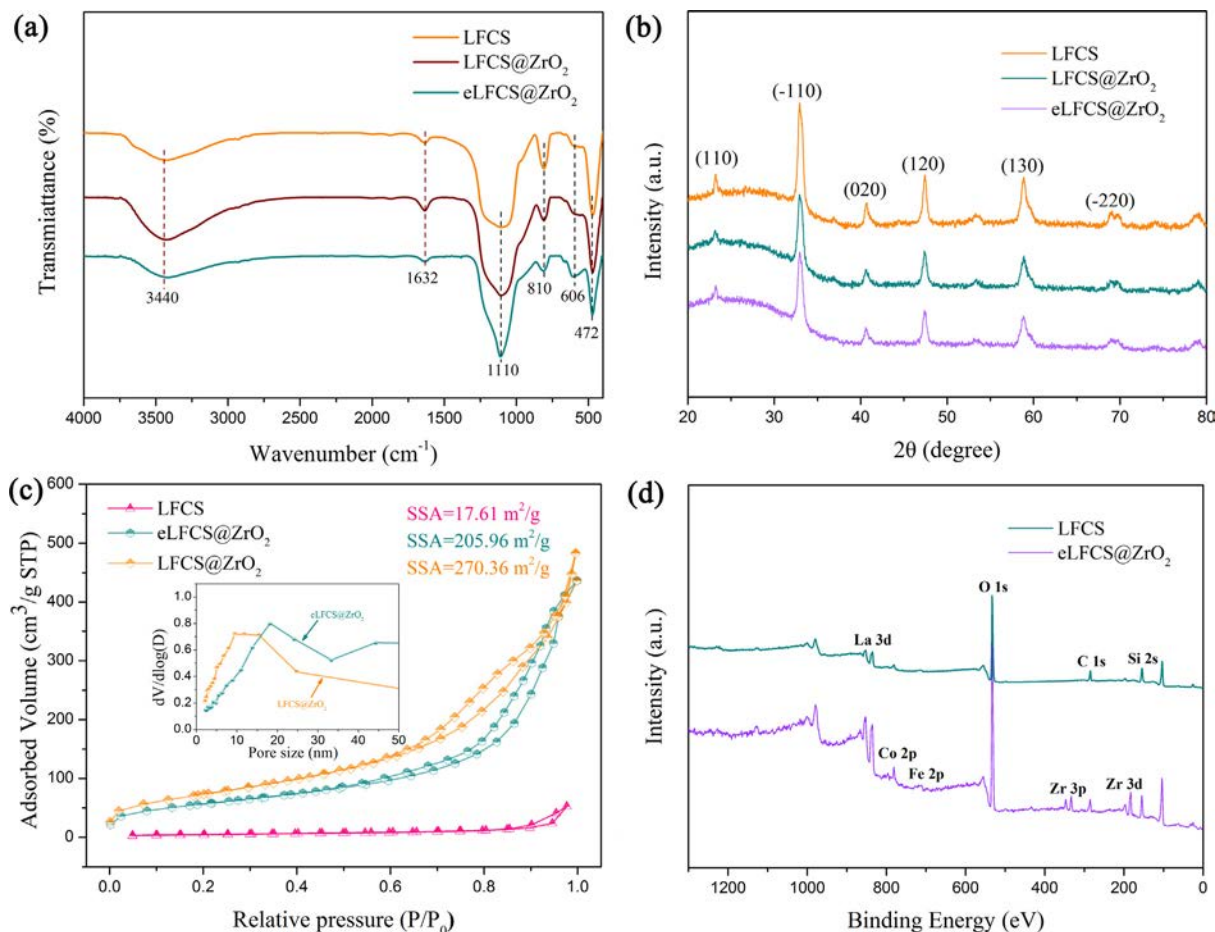
Fig. 2. FT-IR spectrum of functional particles (a); XRD patterns (b); BET analysis (c) and XPS full scale spectrum (d).
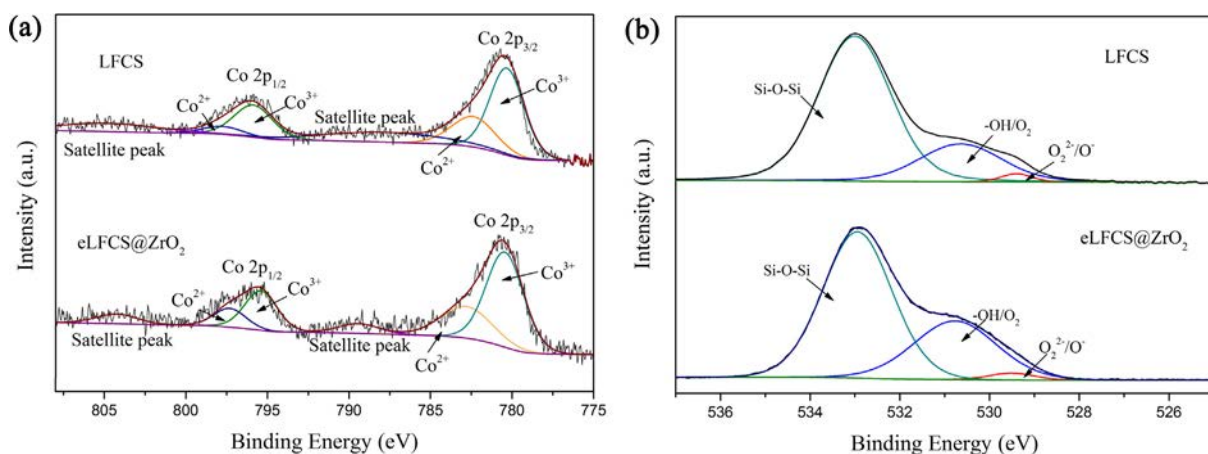

Fig. 3. XPS spectrum of functional particles. Co 2p (a) and O 1s (b).

Therefore, it was inferred that the oxygen vacancy density increased after ZrO_2 coating because of the intrinsic defect properties of ZrO_2. To prove this hypothesis, the O 1s spectrum was identified and is shown in Fig. 3(b). The fine-scanned O 1s spectrum mainly comprised three contributions, the peaks centered at ~532.9, ~530.8, and ~529.6 eV were ascribed to Si-O-Si band and overlapped adsorbed H_2O or CO_3^-, surface hydroxyl (–OH/O_2), and reactive O_2^{2-}/O^- generated form oxygen vacancy, respectively [35]. For LFCS, the relative ratio of these three oxygen peaks was 75.7%, 22.4%, and 1.9%, and changed to 66.0%, 30.9%, and 3.1% for

the etched samples. The relative ratio of the Si-O-Si band decreased owing to the partially hydrolysis process, while the surface hydroxyl and O_2^{2-}/O^- component increased. On the one hand, the increased hydroxyl group facilitated the dispersion of the catalyst in aqueous solution, enhancing the contact between the pollutants and catalysts. On the other hand, the increased O_2^{2-}/O^- concentration proved the increment of oxygen vacancies on the catalyst surface, which could promote the generation of the non-radicals to further accelerate the catalytic oxidation. In addition, the high-resolution XPS spectrums of La, Fe, Zr, and Si are depicted in
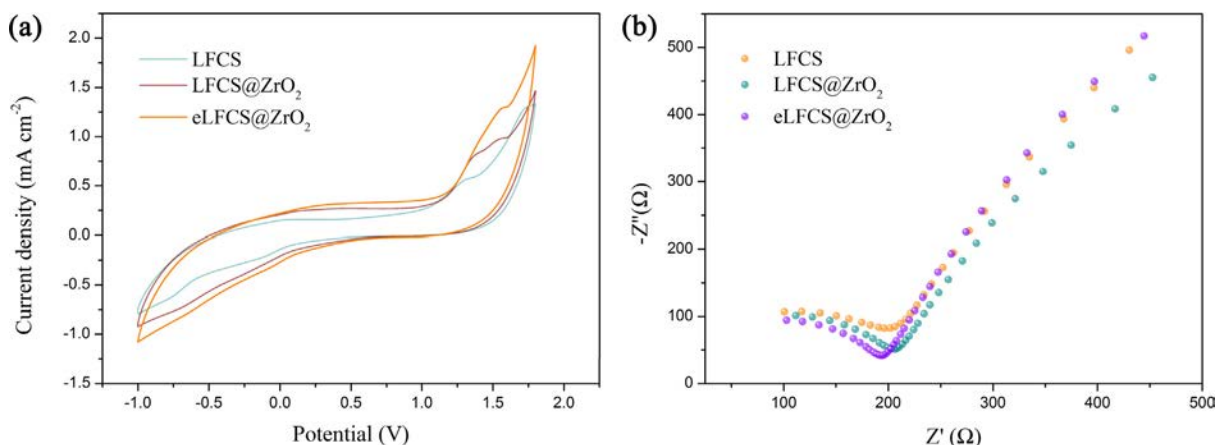
Fig. 4. Electrochemistry measurement of the catalysts. EIS Nyquist plots (a) and CV curves (b).
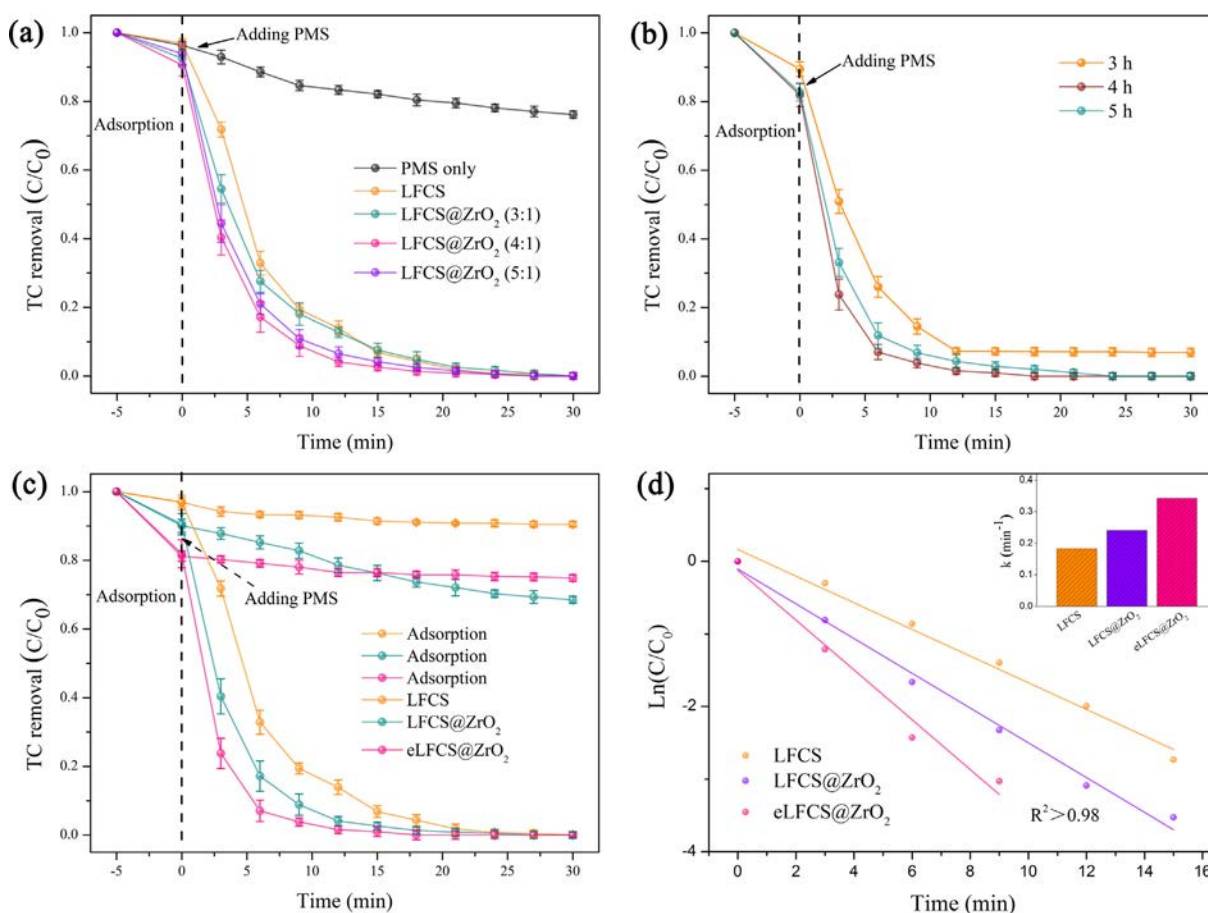

Fig. 5. Catalytic performance of various functional particles toward TC degradation. Effect on ZrO$_2$ coating (a); effect on etching time (b); comparison of functional particles on TC degradation efficiency (c) and constant reaction rate analysis (d). (TC: 20 mg/L; 100 mL, catalyst: 0.1 g/L, PMS concentration: 1 mM, T = 25 °C).

Fig. S4. Two characteristic peaks of eLFCS@ZrO$_2$ located at ~182.5 and ~184.9 eV corresponded to Zr 3d$_{5/2}$ and 3d $_{3/2}$ of ZrO$_2$, proving the formation of the ZrO$_2$ shell [36].

The CV curves of the functional particles are illustrated in Fig. 4 (a), the eLFCS@ZrO$_2$ performed a higher current density than that of other catalysts as well as greater reducibility to coordinate a redox process, which was favorable for the PMS activating progress. As presented in Fig. 5(b), the EIS Nyquist plot of LFCS@ZrO$_2$ showed an increased semicircle diameter when coated by the ZrO$_2$ shell, but exhibited a downtrend when LFCS@ZrO$_2$ was partially

etched by alkaline solution owing to the decrease in SiO$_2$ proportion. The eLFCS@ZrO$_2$ with a smaller semicircle diameter was beneficial for the electron transfer between PMS and catalyst, further promoting the TC degradation process.

3.2. Catalytic performance of functional particles

The catalytic oxidation performance of various functional particles was evaluated by TC degradation. In a typical experiment, 10 mg functional catalyst was added into 100 mL TC aqueous solu-

tion (20 mg/L) under magnetic stirring and the reaction temperature was 25 °C. As for the heterogeneous catalytic reactions, it is well accepted that the initial step is the adsorption of the pollutant on catalyst surface [4]. The adsorption capacities of samples were verified and depicted in Fig. 5(c). The LFCS exhibited negligible adsorption ability, and only 9.5% of the TC was adsorbed on LFCS owing to the low SSA. Besides, when coated with porous ZrO_2 and finished the etching process, the functional particle performed attractive adsorption characters. 31.5% and 25.2% of the TC adsorption were achieved by LFCS@ZrO_2 and eLFCS@ZrO_2 particles, respectively. The adsorption performance is closely related to the surface charge of catalysts. As shown in Fig. S5, the pH_{pzc} of eLFCS@ZrO_2 was about 4.6, and the surface charge was negative when pH varied from 4.6 to 11.0. Accordingly, strong electrostatic interaction can be achieved between negatively charged eLFCS@ZrO_2 and positively charged TC, which facilitated the adsorption of TC on catalysts surface and thus improved catalytic oxidation performance. Notably, adsorption capacity increased obviously in the first 5 min as evidence by the enlarged SSA and size distribution, it was observed that 18.8% of TC was adsorbed on eLFCS@ZrO_2 catalyst while the adsorption capacity of LFCS@ZrO_2 was 10.1%. Based on the above analysis, to further improve the catalytic efficiency and reduce energy consumption, the optimal adsorption time was set as 5 min. The effect on the amount of ZrO_2 coating is shown in Fig. 5(a) and Fig. S6. Initially, it was observed that 23.8% of TC was degraded in the presence of PMS alone because of its thermodynamically oxidation characteristics, which can generate free radicals through weak self-decomposition [10]. Numerous literatures proved that ZrO_2 can hardly react with PMS to generate radicals [4,6]. A comparative experiment was conducted to further prove this perspective. As shown in Fig. S6, the TC removal efficiency of the ZrO_2/PMS system was 45.8%, which was more like the addition of the ZrO_2 adsorption (22.9%) and degradation induced by PMS alone (25.2%). This phenomenon proved that the ZrO_2 can hardly participate in the formation of free radicals. With the addition of the LFCS or LFCS@ZrO_2 under different coating ratio, a significant improvement in TC degradation was observed. Besides, the catalyst with the core-shell structure exhibited better TC degradation efficiency than pristine LFCS. Accordingly, the constant reaction rate gradually increased with the coating amount and decreased after reaching 1:5, and the constant reaction rate was 0.1836, 0.1843, 0.2413, and 0.2089 min^{-1}, respectively. This phenomenon can be explained from two aspects: 1) the thicker shell delayed the contact between the pollutant and PMS on the catalyst surface; 2) a small amount of ZrO_2 coating cannot provide a sufficiently high SSA, which hindered the pollutant adsorption process, and resulted in a decreased catalytic efficiency. The TC degradation ratio reached 95.9% in 15 min and 99% in 30 min as the reaction progress under the core-shell weight ratio (LFCS:ZrO_2 = 4:1), which was considered as the optimal candidate for TC degradation and was employed in the etching process to further improve the catalytic efficiency. As observed in Fig. 5(b), the degradation efficiency increased firstly and then decreased with the extension of etching time, because longer etching time can cause a decreased SSA and thereby damage the catalyst structure. Therefore, the optimal etching time of the eLFCS@ZrO_2 was set as 4 h. The comparison of the various catalysts for TC degradation is shown in Fig. 5(c) and Fig. 5 (d). The eLFCS@ZrO_2 exhibited superior catalytic efficiency, and 95.2% of TC was degraded within 9 min and further reached 99% at 15 min. The constant reaction rates of the LFCS, LFCS@ZrO_2, and eLFCS@ZrO_2 were 0.1836, 0.2413 and 0.3432 min^{-1} respectively, showing the attractive degradation efficiency. More importantly, the reaction kinetic of eLFCS@ZrO_2 was about twice that of LFCS because of the enhanced mass transfer during catalytic oxidation process. The COD was also tested to verify the catalytic perfor-

mance of the eLFCS@ZrO_2. As shown in Table S2, the removal ratio of the COD was 70.1% in 30 min while that for TOC was 51.6%, which performed attractive ability to TC degradation.

The influence of several parameters, for instance, PMS and catalysts dosage, TC concentration, pH, and temperature were investigated. As shown in Fig. 6(a), with the increase of the PMS dosage, the TC degradation efficiency increased firstly and then showed a decreasing trend when PMS dosage reached 1.5 mM. On the one hand, the appropriate PMS dosage can promote the catalytic oxidation process due to the unoccupied active site on the catalyst surface. On the other hand, with the addition of excessive PMS, self-scavenging of PMS was activated to generate SO_5^- with lower oxidative ability, and thus inhibited the TC degradation process [6]. For the dosage of the catalyst (Fig. 6(b)), it was worth nothing that the adsorption ability improved with the increased dosage of catalyst, and TC degradation efficiency increased from 93.8% to 99.5% along with the catalyst dosage increased from 0.05 g/L to 0.1 g/L. Same degradation efficiency was also observed when catalyst dosage reached 0.15 g/L, but the reaction rate reduced in the early stage of the reaction, which was attributed to the limited dispersity when introducing an excess amount of catalyst. In addition, Fig. 6(c) depicted that TC degradation gradually declined with the increase of TC concentration. The influence of pH on TC degradation is shown in Fig. 6(d), and the initial pH significantly affected the TC degradation performance. The degradation performance of TC was obviously constrained under acidic and strong alkaline conditions. Under acidic conditions, HSO_5^- was dominant in PMS and prone to react with H^+, which inhibited the formation of $CoOH^+$, the indispensable intermediate for the formation of reactive radicals, resulting in a decreased catalytic efficiency [20]. Besides, owing to the intrinsic pK_a value of PMS (pK_{a2} = 9.4), the main component of PMS converted to SO_5^{2-} with unsatisfied activity under strongly alkaline conditions [4]. Consequently, the generation of the SO_4^- was restricted, and caused a decreasing trend in catalytic efficiency. Therefore, the most suitable pH range for TC degradation is in neutral and weakly alkaline conditions, which performed similar rapid degradation capacities. Fig. 6(e) demonstrated that the elevated temperature can facilitate the TC degradation performance, which not only provided sufficient energy to promote the production of free radicals by scission of PMS molecular but also reduced the reaction barriers. The activation energy of the catalytic oxidation was calculated through the Arrhenius equation and is shown in Fig. 6(f), and the activation energy was evaluated to be 15.94 kJ/mol, which performed a lower reaction barrier. Besides, the activation energy was higher than that of diffusion-controlled reaction (~10–13 kJ/mol), proving that the degradation rate was mainly determined by intrinsic chemical reactions on catalyst surface rather than mass transfer rate [17]. To verify the influence of the addition ions on catalytic degradation, various anions (Cl^-, HCO_3^-, HPO_4^{2-} and NO_3^-) were introduced to the TC/PMS/catalyst system. As illustrated in Fig. S3, the TC adsorption capacity of the catalyst was suppressed when adding 0.2 mol/L of anions, which was 200 times than PMS concentration. Besides, due to the reaction between anion and PMS, the TC degradation efficiency was further impeded. Among them, divalent HPO_4^{2-} showed a negligible impact on TC degradation, whereas Cl^-, HCO_3^- and NO_3^- demonstrated greater inhibitory effects on account of the lower oxidation capacity of the generated radicals such as ($Cl^.$, HCO_3^- etc.) [37]. In the presence of the 0.2 mol/L NaCl and NaHCO₃, only 80% of TC was removed within 30 min.

3.3. Stability of functional particles

Fig. 7(a) confirmed the cycling abilities of the eLFCS@ZrO_2 toward TC degradation. Results showed that about 91.5% of TC could be eliminated after five consecutive cycles under the same
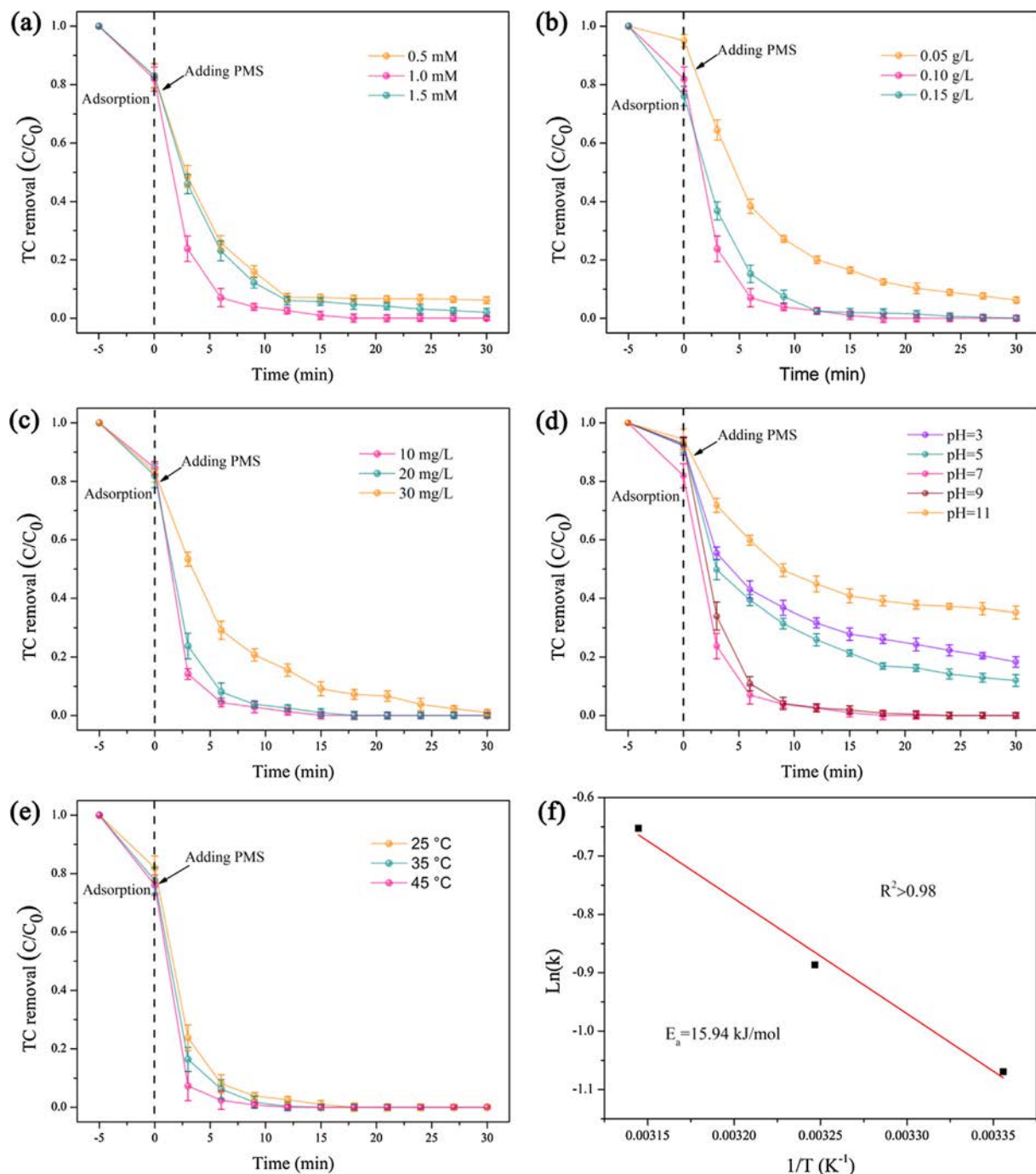
Fig. 6. Effects of various parameters on TC degradation. PMS concentration (a); catalyst dosage (b); TC concentration (c); pH (d); temperature (e) and Arrhenius equation analysis (f). (TC: 20 mg/L; 100 mL, catalyst: 0.1 g/L, PMS concentration: 1 mM, T = 25 °C).

conditions in the first 15 min, indicating favorable stability of the eLFCS@ZrO$_2$. The cobalt ion leaching was also evaluated to test the stability of the functional particles. As illustrated in Fig. 7(b), the cobalt ion leaching of the perovskite was 3.61 mg/L and reduced to 1.53 mg/L when deposited on SiO$_2$ support. Besides, the cobalt ion leaching declined to 0.67 mg/L after coating ZrO$_2$ shell and etching processes, which was lower than the limitation of China (GB-25467-2010, ≤1 mg/L), showing an environmental-friendly performance.

To better verify the stability of the catalyst, the XPS spectrums of the catalyst were analyzed before and after the catalytic oxidation. As illustrated in Fig. 8(a), the Co 2p spectrums of the

eLFCS@ZrO$_2$ before and after reaction were basically constant, except for the no-obvious change in the proportion of Co^{3+} to Co^{2+}. The relative ratio of the Co^{3+} to Co^{2+} was 68.1% and 31.9%, and converted to 70.6% and 29.4%, indicating that the redox pair of Co^{3+}/Co^{2+} participated in the PMS activation process. For the O 1s spectra shown in Fig. 8(b), the proportion of surface hydroxyl (~530.8 eV) decreased from 30.9% to 20.3%, revealing that surface hydroxyl was involved in the TC degradation process by bonding with PMS. Furthermore, the component of O$_2^{2-}$/O$^-$ was almost unchanged. These results indicated that the eLFCS@ZrO$_2$ performed favorable stability.
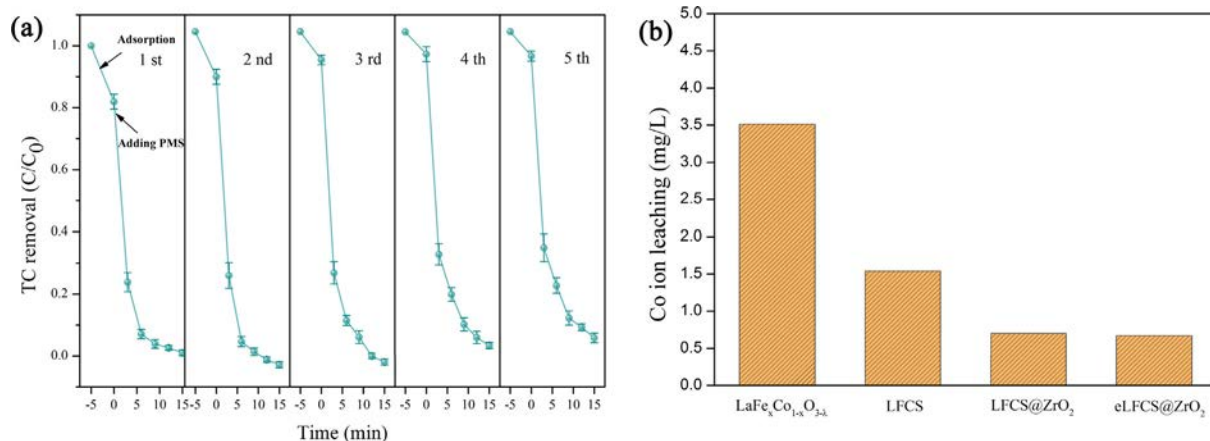
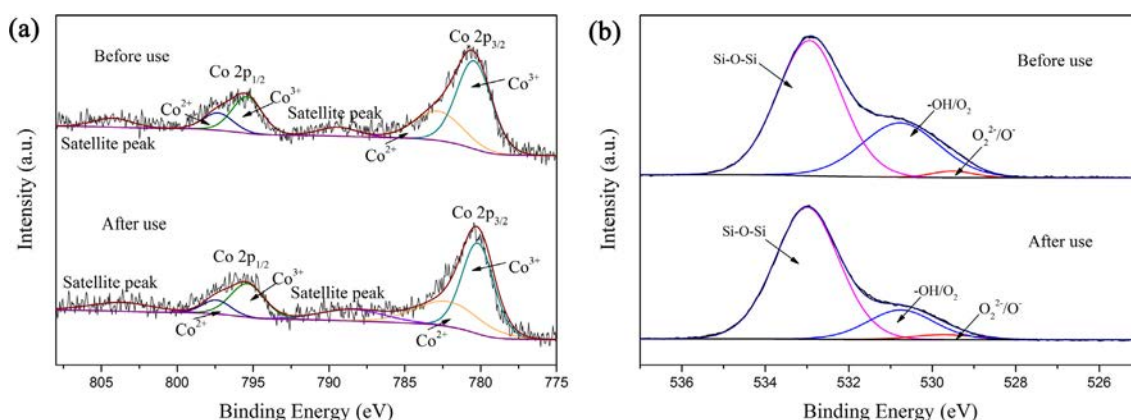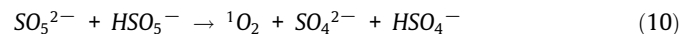**Fig. 7.** Stability of the functional particles (a) and cobalt leaching of functional particles (b).

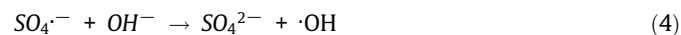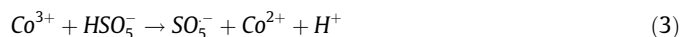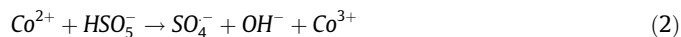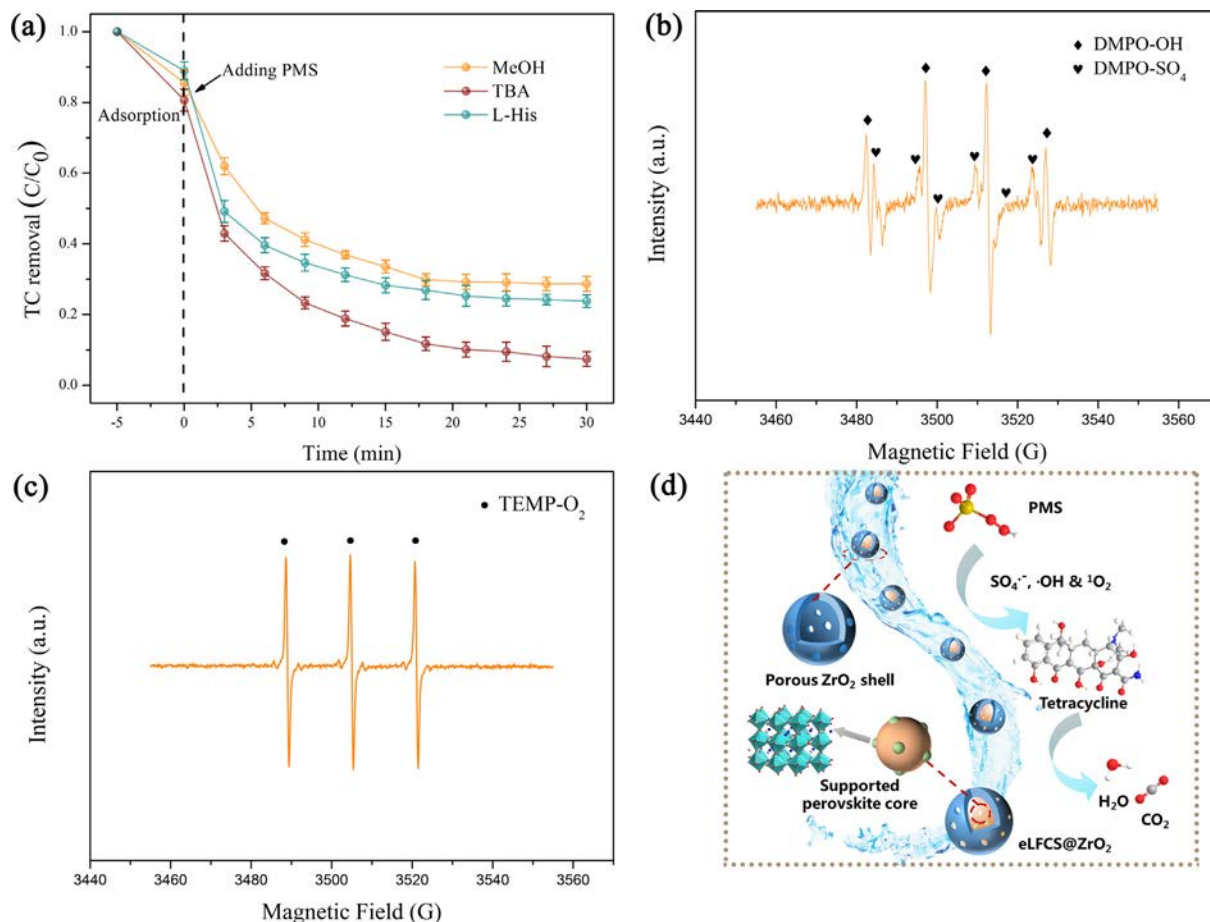**Fig. 8.** XPS spectrum of eLFCS@ZrO$_2$ before and after use. Co 2p (a) and O1 s (b).

3.4. Possible mechanism analysis

It is well known that various free radicals and non-radicals participate in the degradation process of pollutants during catalytic oxidation. To identify the reactive oxygen species and their contributions to the eLFCS@ZrO$_2$/PMS system, MeOH was employed to scavenge both ·OH and SO$_4^-$ because of the reaction rate between MeOH and radicals ($k_{SO4\cdot-+MeOH}$ = (1.6–7.7) × 10^7 M^{-1}S^{-1} and $k_{\cdot OH+-MeOH}$ = (1.2–2.8) × 10^9 M^{-1}S^{-1}). By contrast, TBA was introduced to quench ·OH ($k_{\cdot OH+TBA}$ = (3.8–7.6) × 10^8 M^{-1}S^{-1} $k_{SO4\cdot-+TBA}$ = (4.0–9.1) × 10^5 M^{-1}S^{-1}). As shown in Fig. 9(a), the adsorption ability was inhibited when introducing additional scavengers. In the presence of 0.2 mol/L MeOH (200 folds than that of PMS concentration), the TC degradation efficiency reduced to 71.4% in 30 min. Besides, 93.6% of TC was eliminated in 30 min with the addition of the 0.2 mol/L TBA, which performed a slight downward trend. Therefore, it was deduced that both ·OH and SO$_4^-$ were generated during the degradation process, and in contrast, SO$_4^-$ occupied the main proportion of reactive radicals. Furthermore, L-his was considered to probe the existence of $^1O_2$ (3.2 × 10^7 M^{-1}S^{-1}). Adding 4 mM L-his (4 folds than that of PMS) led to a 76.2% TC removal in 30 min. Apparently, the addition of a small amount of L-his showed an intense effect on TC degradation. To further confirm the reactive oxygen species in eLFCS@ZrO$_2$/PMS system, EPR analyses was carried out using DMPO and TEMP as spin-trapping agents. The characteristic peaks of DMPO-OH (αH = αN = 14.8 G) and DMPO-SO$_4$ (αH = 0.78 G, αH = 14.8 G, αH = 9.6 G, and αN = 13.2 G) adducts with reactive intensities of 1:2:2:1 were observed in Fig. 9 (b),

demonstrating the existence of ·OH and SO$_4^-$. Besides, Fig. 9 (c) exhibited the characteristic 1:1:1 triplet signal of the TEMP-1O2 adduct, which was corresponded to the generation of $^1O_2$ [38]. Therefore, it can be concluded that both radicals and non-radical were involved in the TC degradation process. Based on the above analysis, SO$_4^-$ and $^1O_2$ played a vital role in the catalytic oxidation process.

$$Co^{2+} + HSO_5^- \rightarrow SO_4^- + OH^- + Co^{3+} \tag{2}$$

$$Co^{3+} + HSO_5^- \rightarrow SO_5^- + Co^{2+} + H^+ \tag{3}$$

$$SO_4^{\cdot-} + OH^- \rightarrow SO_4^{2-} + \cdot OH \tag{4}$$

$$Fe^{2+} + HSO_5^- \rightarrow SO_4^- + Fe^{3+} + OH^- \tag{5}$$

$$Fe^{3+} + HSO_5^- \rightarrow SO_5^- + Fe^{2+} + H^+ \tag{6}$$

$$Fe^{2+} + Co^{3+} \rightarrow Co^{2+} + Fe^{3+} \tag{7}$$

$$V_O^{\cdot\cdot} \rightarrow O_o^x \tag{8}$$

$$O_o^x + HSO_5^- \rightarrow {}^1O_2 + HSO_4^- \tag{9}$$

$$SO_5^{2-} + HSO_5^- \rightarrow {}^1O_2 + SO_4^{2-} + HSO_4^- \tag{10}$$

$$TC + \cdot OH/SO_4^{\cdot-}/{}^1O_2 \rightarrow Intermediates \rightarrow CO_2 + H_2O \tag{11}$$
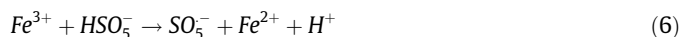
Fig. 9. Possible mechanism of the eLFCS@ZrO$_2$/PMS system. Radical quenching test (a); EPR analysis of SO$_4^-$ and ·OH (b); spectrum of ^{1}O$_2$ (c) and scheme of possible mechanisms (d).

The possible degradation mechanism was proposed in Eqs. (2)–(11). Typically, the degradation process can be divided into the following two aspects: 1) the radical induced degradation pathway and 2) the non-radical pathway. For the radical guided degradation pathway, Co^{2+} can react with HSO$_5^-$ to produce SO$_4^-$ radicals and oxidized to Co^{3+} as Eq. (2). Besides, Co^{3+} can still interact with HSO$_5^-$ to form Co^{2+} and SO$_5^-$ with lower oxidation ability, which completed the redox cycle of Co^{2+} and Co^{3+}. However, owing to a lower reaction rate, Eq. (3) was often regarded as the rate-controlling reaction [6]. Besides, similar to the reaction between cobalt ions and HSO$_5^-$, the doped element Fe can also react with HSO$_5^-$ under the same conditions. Furthermore, Co^{3+}/Co^{2+} performed higher standard reduction potential (1.81 V) than that of Fe^{3+}/Fe^{2+}(0.77 V), and Co^{3+} on catalyst surface can be reduced to Co^{2+} by reacting with Fe^{2+} as shown in Eq. (7), which accelerated the electron transfer and was favorable to promote TC degradation process. Moreover, non-radical ^{1}O$_2$ can be generated from oxygen vacancies (V$_o^{..}$) from catalyst structure through Eq. (8) and (9). Besides, ^{1}O$_2$ can also be produced by the reaction between HSO$_5^-$ and SO$_5^{2-}$ as depicted in Eq. (10). Finally, TC was oxidized by the radicals and non-radicals to produce a series of intermediates and gradually mineralized to H$_2$O and CO$_2$ as the reaction progressed.

The possible TC degradation pathways were proposed in Fig. 10. Three intermediates with m/z = 446, 453, and 435 were generated through cleavage of the functional groups, hydroxylation, and dehydration process. Besides, the intermediate was further oxidized to P4 to P6 with m/z = 362, 342, and 322 via the hydroxyla-

tion and carboxylation processes. Afterwards, the ring-opening reaction was dominated in the degradation process and formed P7 to P10 with relatively low molecular weight, and further oxidized through hydroxylation and demethylation to form P11 and P12. Furthermore, P13 and P14 with m/z = 88 and 74 were formed through further ring-opening reactions and finally mineralized to CO$_2$ and H$_2$O to achieve the TC degradation process.

The comparison of the catalytic efficiency and cobalt ion leaching in this work and various cobalt-based perovskite are listed in Table 1. A relative high cobalt ion leaching is observed of various cobalt-based perovskite. Among them, the core-shell structured eLFCS@ZrO$_2$ exhibits favorable catalytic efficiency and limited cobalt ion leaching, showing an eco-friendly character. Therefore, the eLFCS@ZrO$_2$ can be further applied in wastewater remediation.

4. Conclusions

In this study, a novel core-shell structured eLFCS@ZrO$_2$ was fabricated and used to degrade organic pollutants via activating PMS. The eLFCS@ZrO$_2$ performed better catalytic efficiency as well as suppressed cobalt ion leaching compared with pristine perovskite LaFe$_{0.1}$Co$_{0.9}$O$_{3-\lambda}$. Results showed that the eLFCS@ZrO$_2$ exhibited favorable catalytic efficiency toward TC (99% in 15 min) as well as suppressed Co leaching (0.67 mg/L), demonstrating high catalytic efficiency and environmentally friendly characteristics compared with other related works toward perovskite-based catalysts (Table 1). Besides, radical quenching test and EPR analysis proved
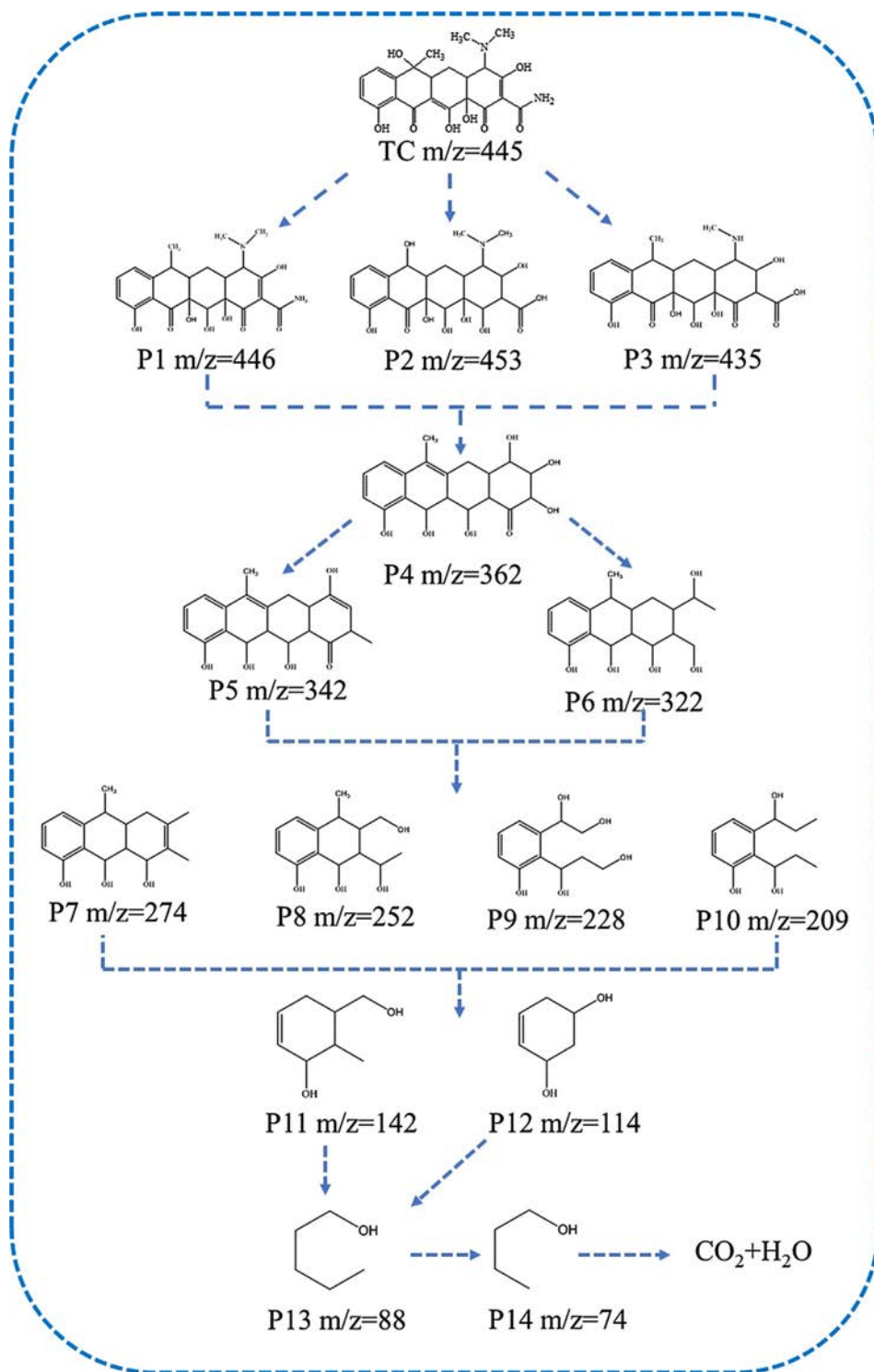
Fig. 10. Analysis of the possible TC degradation pathways.

that both SO_4^- and $^1O_2$ were involved in the TC degradation process. Furthermore, the cycling test indicated that the eLFCS@ZrO$_2$ exhibited favorable stability after 5 consecutive cycles. Therefore, this work provides a promising strategy for the rational design and application of functional catalysts for wastewater remediation.

CRediT authorship contribution statement

Longfei Zhang: Conceptualization, Methodology, Validation, Formal analysis, Investigation, Data curation, Writing - original draft, Writing - review & editing, Visualization. **Luhong Zhang:**

Table 1
The catalytic activities of various cobalt-based perovskite material in SR-AOPs.

Catalyst	Target pollutant	Operation conditions	Results	Ref.
$SrCo_{0.6}Ti_{0.4}O_{3-\delta}$@CoOOH	Phenol (20 mg/L)	PMS: 2.0 g/L Catalyst: 0.06 g/L Temperature:25 °C	Removal:100% (20 min) Cobalt leaching: 4.97 mg/L	[35]
$LaCoO_3$-SiO_2	PBSA (5 mg/L)	PMS: 5.0 mM Catalyst: 0.5 g/L Temperature:25 °C	Removal:100% (10 min) Cobalt leaching: 2.69 mg/L	[39]
$LaCo_{1-x}Mn_xO_{3+\delta}$	Phenol (20 mg/L)	PMS: 6.5 mM Catalyst: 0.1 g/L Temperature:25 °C	Removal:100% (60 min) Cobalt leaching: 3.97 mg/L	[40]
$La_2CoMnO_{6-\delta}$	Atrazine (~2 mg/L)	PMS: 1.0 mM Catalyst: 0.1 g/L Temperature:25 °C	Removal:99% (60 min) Cobalt leaching: 2.49 mg/L	[41]
$LaCo_{1-x}Cu_xO_3$	Phenol (20 mg/L)	PMS: 0.2 g/L Catalyst: 0.1 g/L Temperature:25 °C	Removal:100% (12 min) Cobalt leaching:1.37 mg/L	[17]
$SrCoO_3$	Phenol (20 mg/L)	PMS: 0.1 g/L Catalyst: 0.3 g/L Temperature: 25 °C	Removal: 100% (120 min) Cobalt leaching: 1.17 mg/L	[19]
$PrBaCo_2O_{5+\delta}$	Phenol (20 mg/L)	PMS: 2.0 g/L Catalyst: 0.1 g/L Temperature:25 °C	Removal: 100% (20 min) Cobalt leaching: 1.70 mg/L	[34]
$eLFCS$@ZrO_2	TC (20 mg/L)	PMS: 1.0 mM Catalyst: 0.1 g/L Temperature:25 °C	Removal: ≥99% (15 min) Cobalt leaching: 0.67 mg/L	This work

*Abbreviation: 2-phenyl-5-sulfobenzimidazole acid (PBSA); benzotriazole (BZA); tetracycline hydrochloride (TC).

Validation, Supervision, Project administration, Visualization, Funding acquisition. **Yongli Sun:** Validation, Supervision, Project administration, Funding acquisition. **Bin Jiang:** Validation, Supervision, Project administration, Funding acquisition.

Declaration of Competing Interest

The authors declare that they have no known competing financial interests or personal relationships that could have appeared to influence the work reported in this paper.

Acknowledgments

Appendix A. Supplementary material

Supplementary data to this article can be found online at https://doi.org/10.1016/j.jcis.2021.03.171.

References

[1] B.C. Hodges, E.L. Cates, J.-H. Kim, Challenges and prospects of advanced oxidation water treatment processes using catalytic nanomaterials, Nat. Nanotechnol. 13 (8) (2018) 642–650.

[2] M.S. Mauter, I. Zucker, F. Perreault, J.R. Werber, J.-H. Kim, M. Elimelech, The role of nanotechnology in tackling global water challenges, Nat. Sustain. 1 (4) (2018) 166–175.

[3] F. Liu, J. Cao, Z. Yang, W. Xiong, Z. Xu, P. Song, M. Jia, S. Sun, Y. Zhang, X. Zhong, Heterogeneous activation of peroxymonosulfate by cobalt-doped MIL-53(Al) for efficient tetracycline degradation in water: Coexistence of radical and non-radical reactions, J. Colloid Interface Sci. 581 (2021) 195–204.

[4] W.-D. Oh, Z. Dong, T.-T. Lim, Generation of sulfate radical through heterogeneous catalysis for organic contaminants removal: Current development, challenges and prospects, Appl. Catal. B 194 (2016) 169–201.

[5] Y. Zhao, D.i. Wu, Y. Chen, Y. Li, X. Fan, F. Zhang, G. Zhang, W. Peng, Thermal removal of partial nitrogen atoms in N-doped graphene for enhanced catalytic oxidation, J. Colloid Interface Sci. 585 (2021) 640–648.

[6] S. Wacławek, H.V. Lutze, K. Grübel, V.V.T. Padil, M. Černík, D.D. Dionysiou, Chemistry of persulfates in water and wastewater treatment: A review, Chem. Eng. J. 330 (2017) 44–62.

[7] R. Xiao, Z. Luo, Z. Wei, S. Luo, R. Spinney, W. Yang, D.D. Dionysiou, Activation of peroxymonosulfate/persulfate by nanomaterials for sulfate radical-based advanced oxidation technologies, Curr. Opin. Chem. Eng. 19 (2018) 51–58.

[8] Y. Ji, Y. Shi, L. Wang, J. Lu, Denitration and renitration processes in sulfate radical-mediated degradation of nitrobenzene, Chem. Eng. J. 315 (2017) 591–597.

[9] X. Dong, X. Duan, Z. Sun, X. Zhang, C. Li, S. Yang, B. Ren, S. Zheng, D.D. Dionysiou, Natural illite-based ultrafine cobalt oxide with abundant oxygen-vacancies for highly efficient Fenton-like catalysis, Appl. Catal. B 261 (2020) 118214.

[10] P. Hu, M. Long, Cobalt-catalyzed sulfate radical-based advanced oxidation: A review on heterogeneous catalysts and applications, Appl. Catal. B 181 (2016) 103–117.

[11] Q. Zhang, D. He, X. Li, W. Feng, C. Lyu, Y. Zhang, Mechanism and performance of singlet oxygen dominated peroxymonosulfate activation on CoOOH nanoparticles for 2,4-dichlorophenol degradation in water, J. Hazard. Mater. 384 (2020) 121350.

[12] M. Abdul Nasir Khan, P. Kwame Klu, C. Wang, W. Zhang, R. Luo, M. Zhang, J. Qi, X. Sun, L. Wang, J. Li, Metal-organic framework-derived hollow Co_3O_4/carbon as efficient catalyst for peroxymonosulfate activation, Chem. Eng. J. 363 (2019) 234–246.

[13] N. Zhou, J. Zu, L. Yang, X. Shu, J. Guan, Y. Deng, D. Gong, C. Ding, M.-E. Zhong, Cobalt (0/II) incorporated N-doped porous carbon as effective heterogeneous peroxymonosulfate catalyst for quinclorac degradation, J. Colloid Interface Sci. 563 (2020) 197–206.

[14] J. Miao, X. Duan, J. Li, J. Dai, B. Liu, S. Wang, W. Zhou, Z. Shao, Boosting performance of lanthanide magnetism perovskite for advanced oxidation through lattice doping with catalytically inert element, Chem. Eng. J. 355 (2019) 721–730.

[15] Y. Yao, Y. Cai, G. Wu, F. Wei, X. Li, H. Chen, S. Wang, Sulfate radicals induced from peroxymonosulfate by cobalt manganese oxides ($Co_xMn_{3-x}O_4$) for Fenton-Like reaction in water, J. Hazard. Mater. 296 (2015) 128–137.

[16] Y. Zhou, Y. Zhang, X. Hu, Novel zero-valent Co–Fe encapsulated in nitrogen-doped porous carbon nanocomposites derived from $CoFe_2O_4$@ZIF-67 for boosting 4-chlorophenol removal via coupling peroxymonosulfate, J. Colloid Interface Sci. 575 (2020) 206–219.

[17] S. Lu, G. Wang, S. Chen, H. Yu, F. Ye, X. Quan, Heterogeneous activation of peroxymonosulfate by $LaCo_{1-x}Cu_xO_3$ perovskites for degradation of organic pollutants, J. Hazard. Mater. 353 (2018) 401–409.

[18] J. Zhu, H. Li, L. Zhong, P. Xiao, X. Xu, X. Yang, Z. Zhao, J. Li, Perovskite Oxides: Preparation, Characterizations, and Applications in Heterogeneous Catalysis, ACS Catal. 4 (2014) 2917–2940.

[19] S.B. Hammouda, F. Zhao, Z. Safaei, V. Srivastava, D. Lakshmi Ramasamy, S. Iftekhar, S. kalliola, M. Sillanpää, Degradation and mineralization of phenol in aqueous medium by heterogeneous monopersulfate activation on nanostructured cobalt based-perovskite catalysts $ACoO_3$ (A = La, Ba, Sr and Ce): Characterization, kinetics and mechanism study, Appl. Catal. B 215 (2017) 60–73.

[20] L. Zhang, Y. Zhang, J. Wei, W. Liu, Perovskite $LaFe_xCo_{1-x}O_{3-\lambda}$ deposited SiO_2 catalytic membrane for deeply cleaning wastewater, Chem. Eng. J. 403 (2021) 126386.

[21] P. Shi, X. Dai, H. Zheng, D. Li, W. Yao, C. Hu, Synergistic catalysis of Co_3O_4 and graphene oxide on Co_3O_4/GO catalysts for degradation of Orange II in water by advanced oxidation technology based on sulfate radicals, Chem. Eng. J. 240 (2014) 264–270.

[22] S. He, C. Yan, X.-Z. Chen, Z. Wang, T. Ouyang, M.-L. Guo, Z.-Q. Liu, Construction of core-shell heterojunction regulating α-Fe_2O_3 layer on CeO_2 nanotube arrays enables highly efficient Z-scheme photoelectrocatalysis, Appl. Catal. B 276 (2020) 119138, https://doi.org/10.1016/j.apcatb.2020.119138.

[23] M. Wang, Y. Cui, H. Cao, P. Wei, C. Chen, X. Li, J. Xu, G. Sheng, Activating peroxydisulfate with Co_3O_4/$NiCo_2O_4$ double-shelled nanocages to selectively degrade bisphenol A – A nonradical oxidation process, Appl. Catal. B 282 (2021) 119585, https://doi.org/10.1016/j.apcatb.2020.119585.

[24] S. Zhang, H. Gao, X. Xu, R. Cao, H. Yang, X. Xu, J. Li, MOF-derived CoN/N-C@SiO_2 yolk-shell nanoreactor with dual active sites for highly efficient catalytic advanced oxidation processes, Chem. Eng. J. 381 (2020) 122670, https://doi.org/10.1016/j.cej.2019.122670.

[25] M. Zhang, C. Wang, C. Liu, R. Luo, J. Li, X. Sun, J. Shen, W. Han, L. Wang, Metal–organic framework derived Co_3O_4/C@SiO_2 yolk–shell nanoreactors with enhanced catalytic performance, J. Mater. Chem. A 6 (24) (2018) 11226–11235.

[26] T. Zeng, X. Zhang, S. Wang, H. Niu, Y. Cai, Spatial confinement of a Co_3O_4 catalyst in hollow metal-organic frameworks as a nanoreactor for improved degradation of organic pollutants, Environ. Sci. Technol. 49 (2015) 2350–2357.

[27] G. Li, Z. Tang, Noble metal nanoparticle@metal oxide core/yolk–shell nanostructures as catalysts: recent progress and perspective, Nanoscale 6 (2014) 3995–4011.

[28] S.A. Akhade, A. Winkelman, V. Lebarbier Dagle, L. Kovarik, S.F. Yuk, M.-S. Lee, J. Zhang, A.B. Padmaperuma, R.A. Dagle, V.-A. Glezakou, Y. Wang, R. Rousseau, Influence of Ag metal dispersion on the thermal conversion of ethanol to butadiene over Ag-ZrO_2/SiO_2 catalysts, J. Catal. 386 (2020) 30–38.

[29] Y. Sun, B. Wang, N. Yang, X. Tantai, X. Xiao, H. Dou, L. Zhang, B. Jiang, D. Wang, Synthesis of RGO-Supported Molybdenum Carbide (Mo_2C-RGO) for Hydrogen Evolution Reaction under the Function of Poly (Ionic Liquid), Ind. Eng. Chem. Res. 58 (2019) 8996–9005.

[30] Y. Sun, F. Peng, L. Zhang, B. Jiang, H. Dou, N. Zhang, M. Xu, N. Yang, Hierarchical Nitrogen-doped Mo_2C Nanoparticle-in-microflower Electrocatalyst: in Situ Synthesis and Efficient Hydrogen-evolving Performance in Alkaline and Acidic Media, ChemCatChem 12 (2020) 6040–6049.

[31] Y. Zhang, L. Pan, C. Gao, Y. Zhao, Synthesis of ZrO_2–SiO_2 mixed oxide by alcohol-aqueous heating method, J. Sol-Gel Sci. Technol. 58 (2) (2011) 572–579.

[32] L. Chen, Y. Zhang, C. Ma, Perovskites $Sr_xLa_{1-x}Mn_yCo_{1-y}O_{3-\delta}$ coated on Ti as stable non-noble anode for efficient electrocatalytic oxidation of organic wastewater containing ammonia nitrogen, Chem. Eng. J. 393 (2020) 124514, https://doi.org/10.1016/j.cej.2020.124514.

[33] Yangang Wang, Jiawen Ren, Yanqin Wang, Fengyuan Zhang, Xiaohui Liu, Yun Guo, Guanzhong Lu, Nanocasted Synthesis of Mesoporous $LaCoO_3$ Perovskite with Extremely High Surface Area and Excellent Activity in Methane Combustion, J. Phys. Chem. C 112 (39) (2008) 15293–15298.

[34] C. Su, X. Duan, J. Miao, Y. Zhong, W. Zhou, S. Wang, Z. Shao, Mixed Conducting Perovskite Materials as Superior Catalysts for Fast Aqueous-Phase Advanced Oxidation: A Mechanistic Study, ACS Catal. 7 (1) (2017) 388–397.

[35] M. Zhu, J. Miao, X. Duan, D. Guan, Y. Zhong, S. Wang, W. Zhou, Z. Shao, Postsynthesis Growth of CoOOH Nanostructure on $SrCo_{0.6}Ti_{0.4}O_{3-\delta}$ Perovskite Surface for Enhanced Degradation of Aqueous Organic Contaminants, ACS Sustainable Chem. Eng. 6 (11) (2018) 15737–15748.

[36] K.A. Lin, Y.C. Chen, T.Y. Lin, H. Yang, Lanthanum cobaltite perovskite supported on zirconia as an efficient heterogeneous catalyst for activating Oxone in water, J. Colloid Interface Sci. 497 (2017) 325–332.

[37] F. Ghanbari, M. Moradi, Application of peroxymonosulfate and its activation methods for degradation of environmental organic pollutants: Review, Chem. Eng. J. 310 (2017) 41–62.

[38] X. Wang, X. Lu, Z. Zhao, H. Zhong, Z. Zhu, W. Chen, In situ stable growth of β-FeOOH on g-C_3N_4 for deep oxidation of emerging contaminants by photocatalytic activation of peroxymonosulfate under solar irradiation, Chem. Eng. J. 400 (2020) 125872.

[39] X. Pang, Y. Guo, Y. Zhang, B. Xu, F. Qi, $LaCoO_3$ perovskite oxide activation of peroxymonosulfate for aqueous 2-phenyl-5-sulfobenzimidazole degradation: Effect of synthetic method and the reaction mechanism, Chem. Eng. J. 304 (2016) 897–907.

[40] J. Miao, J. Sunarso, X. Duan, W. Zhou, S. Wang, Z. Shao, Nanostructured Co-Mn containing perovskites for degradation of pollutants: Insight into the activity and stability, J. Hazard. Mater. 349 (2018) 177–185.

[41] X. Luo, L. Bai, J. Xing, X. Zhu, D. Xu, B. Xie, Z. Gan, G. Li, H. Liang, Ordered Mesoporous Cobalt Containing Perovskite as a High-Performance Heterogeneous Catalyst in Activation of Peroxymonosulfate, ACS Appl. Mater. Interfaces 11 (2019) 35720–35728.